

pubs.acs.org/cm Article

# Coherent Spin Dynamics in Vapor-Deposited CsPbBr<sub>3</sub> Perovskite Thin Films

Laura M. Jacoby, Matthew J. Crane, and Daniel R. Gamelin\*



Cite This: https://doi.org/10.1021/acs.chemmater.1c04382



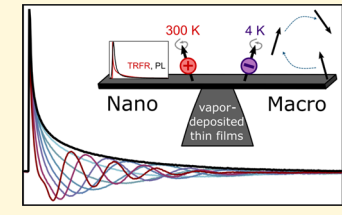
**ACCESS** I

Metrics & More

Article Recommendations

SI Supporting Information

ABSTRACT: Metal-halide perovskite (MHP) thin films show promise for integration into optoelectronic and spin-based devices. Here, we investigate spin dephasing in vapor-deposited  $CsPbBr_3$  thin films via a combination of time-resolved Faraday rotation and magnetic circular dichroism spectroscopy. We observe coherent precession of both photogenerated electron and hole spins. For photogenerated holes, spin-dephasing times  $(T_2^*)$  can be elongated at cryogenic temperatures from 282 to 320 ps by application of a small magnetic field, which partially suppresses hyperfine dephasing. At elevated temperatures, hole-spin dephasing is accelerated by thermally excited longitudinal-optical phonons, but coherent hole-spin precession is still



measurable at room temperature. Photogenerated electrons show rapid spin dephasing ( $\sim$ 40 ps) even at cryogenic temperatures. These results highlight that vapor-deposited CsPbBr<sub>3</sub> thin films offer a compelling platform for harnessing spins in MHP semiconductors, and their scalable manufacturing offers an attractive pathway to future device integration.

Metal-halide perovskites (MHPs) have emerged as a promising family of semiconductors for spintronic and quantum-information applications due to their remarkable optical, electronic, and magneto-electronic properties, which include large spin—orbit coupling, Rashba—Dresselhaus effects, long carrier-diffusion lengths, photostability, spin-dependent optical selection rules, and long optical coherence times.  $^{1-7}$  In addition, MHPs show reasonably long ensemble spin-dephasing times,  $T_2^*$ , a figure of merit for spin-based electronic and quantum-information applications. Some of these advantageous properties were recently exploited to demonstrate spin-based light-emitting diodes from both CsPbBr<sub>3</sub> nanocrystals at room temperature and hybrid organic—inorganic MHP thin films at cryogenic temperatures.  $^{13}$ 

All-inorganic MHP thin films are particularly promising for some applications due to their environmental stability, chemically tunable band gaps that span the visible spectrum, and enhanced charge transport compared to hybrid organicinorganic thin films or nanocrystal MHPs. 14,15 Among other attractive features, all-inorganic MHP thin films can be deposited via physical vapor deposition, a process compatible with very large-scale integration manufacturing. 16,17 To date, however, spin-coherence dynamics have not been investigated in vapor-deposited all-inorganic MHP thin films. In nanocrystalline<sup>9,10</sup> and "single-crystal" CsPbBr<sub>3</sub>, low-temperature spin dephasing was reported to be dominated by nuclear hyperfine interactions, but substantial differences were apparent, including a strong field-induced enhancement of  $T_2^*$  in nanocrystals but not in the single crystal. While nanocrystals show high photoluminescence quantum yields (PLQYs), single crystals show low PL associated with abundant trapping. Nanocrystals show room-temperature spin precession,<sup>9</sup> but the single crystal shows spin precession

only below 100 K.<sup>8</sup> Single-crystal CsPbBr<sub>3</sub> further showed spatially inhomogeneous spin dephasing not observed in nanocrystal samples, attributed to heterogeneous carrier localization effects.<sup>8</sup> MHP thin films are bulk materials but have granular morphologies, and it is unclear how their enhanced mobility relative to nanocrystals, unpassivated grain boundaries, and the absence of surface ligands may impact spin coherence.<sup>18</sup> A very recent comparison of CsPbBr<sub>3</sub> nanocrystals and a solution-deposited polycrystalline film observed only slight differences in g factors and spin dynamics, suggesting that carrier confinement plays a small role, but in both samples, the TRFR signals were attributed to the spins of resident carriers rather than photogenerated carriers.<sup>10</sup> More detailed studies are thus required to understand and control spin coherences in this device-relevant MHP morphology.

In this study, we use magneto-optical spectroscopies to measure temperature- and field-dependent spin dynamics and spin splittings in vapor-deposited CsPbBr<sub>3</sub> thin films. Using time-resolved Faraday rotation (TRFR), we observe coherent precession of both photogenerated electron and hole spins. Magnetic circular dichroism (MCD) spectroscopy shows that these TRFR signals are consistent with band-edge carriers as found in excitons, and the combination of MCD with TRFR directly yields the electron and hole g value signs. From variable-temperature TRFR measurements, photogenerated

Received: December 21, 2021 Revised: January 27, 2022



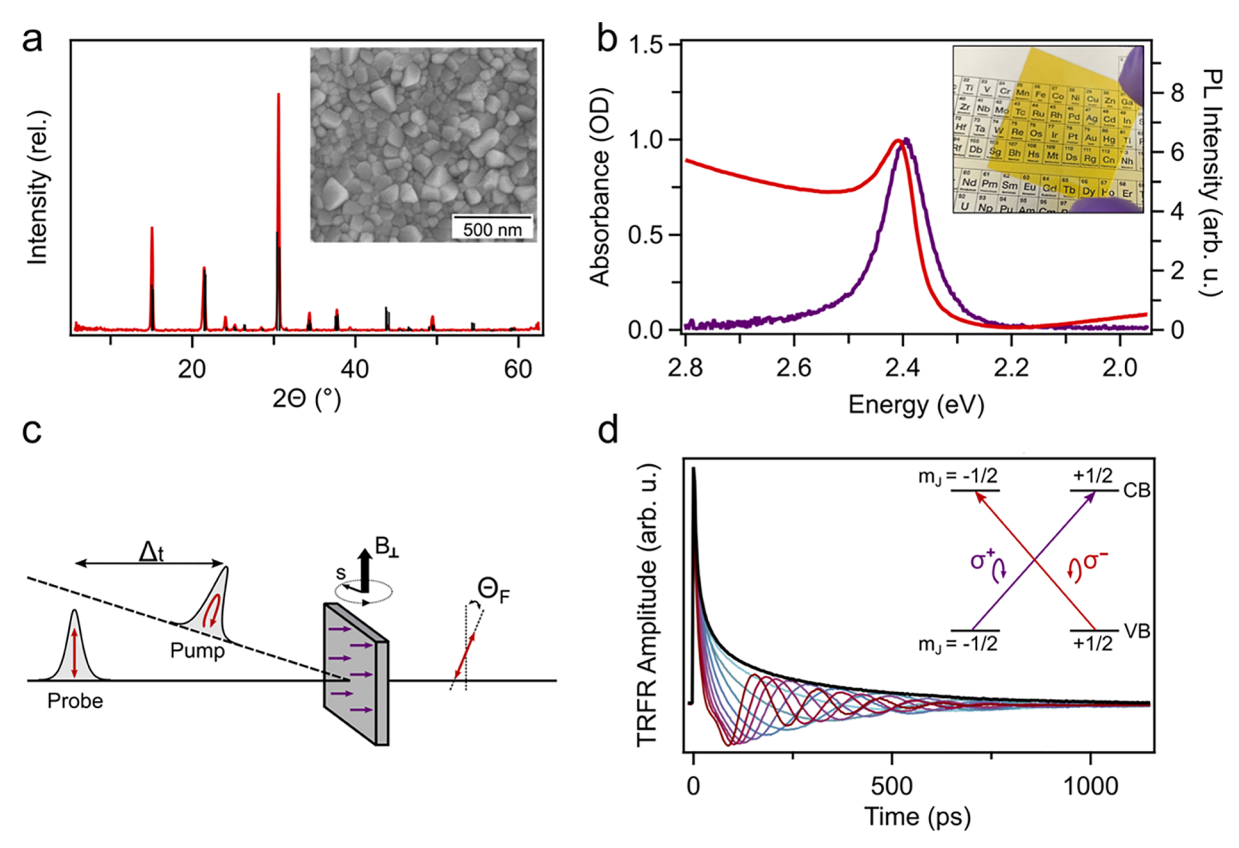


Figure 1. (a) Room-temperature XRD data for the vapor-deposited CsPbBr<sub>3</sub> thin film used in this work. Reference indices are shown for orthorhombic CsPbBr<sub>3</sub>. The inset shows an SEM image of a representative CsPbBr<sub>3</sub> thin film, illustrating crystal domain sizes of  $60 \pm 30$  nm. (b) Room-temperature absorption and PL spectra of vapor-deposited CsPbBr<sub>3</sub> thin films. The inset shows a color photograph of a representative  $1'' \times 1''$  CsPbBr<sub>3</sub> thin film, emphasizing its good optical quality. Interference fringes are observed below the first absorption maximum (see the Supporting Information). (c) Schematic summary of the time-resolved Faraday rotation (TRFR) experiment, in which electron and hole spins are generated along the laboratory z axis using a circularly polarized pump pulse. The sample sits in a transverse magnetic field ( $B_{\perp}$ ), which causes these photogenerated spins to precess. This precession and the spin-coherence decay dynamics are read out *via* Faraday rotation of a time-delayed, linearly polarized probe pulse at the same wavelength. (d) CsPbBr<sub>3</sub> thin-film TRFR time traces measured at 4.5 K under increasing applied transverse magnetic fields (blue to maroon trace,  $E_{\text{pump}} = E_{\text{probe}} = 2.35 \text{ eV}$  (528 nm)). The decay envelopes of the oscillating signals closely follow the zero-field Faraday rotation amplitude decay (black). The inset illustrates the momentum-conserving optical transitions at the band-edge along the optical axis (z) for LCP ( $\sigma^-$ ) and RCP ( $\sigma^+$ ) excitation, from which the spin populations are established.

electron spins are found to dephase rapidly at cryogenic temperatures and are not observed above cryogenic temperatures, whereas photogenerated hole spins precess coherently up to room temperature. Hole-spin dephasing occurs in two distinct regimes: At low temperatures, spin dephasing is accelerated by inhomogeneous hyperfine fields and  $T_2^*$  can be elongated by application of a small magnetic field, similar to nanocrystalline CsPbBr<sub>3</sub>.9 At higher temperatures, excitonphonon coupling drives spin dephasing. Comparison of these results to those from single-crystal and nanocrystalline CsPbBr3 highlights vapor-deposited CsPbBr3 thin films as a bulk MHP that retains the thermally robust spin coherence previously observed only in CsPbBr<sub>3</sub> nanocrystals.<sup>9</sup> These results, combined with the scalability of vapor-deposited thinfilm manufacturing, make CsPbBr3 thin films particularly promising for both fundamental and applied spin-based optoelectronics involving MHPs.

# ■ RESULTS AND DISCUSSION

Synthesis and Characterization of CsPbBr<sub>3</sub> Thin Films. Figure 1a shows X-ray diffraction (XRD) data collected for a representative vapor-deposited CsPbBr<sub>3</sub> thin film. These data are consistent with orthorhombic CsPbBr<sub>3</sub>, and the data

show no signs of preferred growth directions or of other crystalline impurity phases.<sup>19</sup> The inset shows a scanning electron microscopy (SEM) image of a representative thin film, revealing grains with edge-length dimensions of  $60 \pm 30$  nm (see the Supporting Information for edge-length analysis). Figure 1b plots room-temperature absorption and photoluminescence (PL) spectra of a representative vapor-deposited CsPbBr<sub>3</sub> thin film. The inset of Figure 1b shows a color photograph of a 1" × 1" vapor-deposited CsPbBr<sub>3</sub> thin film, illustrating its uniformity and high optical quality. The film has a bright yellow hue and high optical transmission below its absorption threshold, highlighted by the clarity of the image behind the film. The sharp absorption maximum at 2.41 eV corresponds to the first excitonic transition of CsPbBr<sub>3</sub>. The PL maximum (2.39 eV) is slightly Stokes-shifted, likely reflecting reabsorption effects. The absorption spectrum shows interference fringes within the optical gap, from which a film thickness of ~250 nm is estimated.

**TRFR and g Value Analysis.** Figure 1c shows a schematic representation of the TRFR measurement.  $^{20-22}$  In this experiment, a circularly polarized pump pulse produces a transient spin-polarized population of charge carriers. The evolution of these photogenerated spins can be monitored in

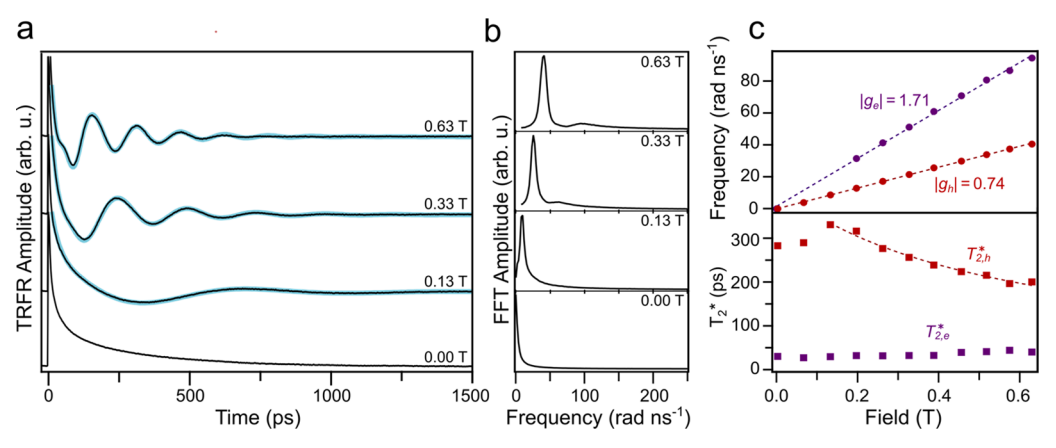


Figure 2. Spin dynamics in a vapor-deposited CsPbBr<sub>3</sub> thin film, measured at 4.5 K. (a) CsPbBr<sub>3</sub> TRFR signals (black) measured at different applied transverse magnetic fields. The oscillation frequency increases with increasing the applied magnetic field, and at the highest fields, two components can be observed. Fits to the data using eq 1 are shown in blue for curves collected with an applied field >0. In the absence of a magnetic field, the data are fit with a biexponential decay function (not shown). (b) Fast Fourier transforms (FFTs) of the TRFR traces from panel (a) show a dominant, low-frequency component associated with photogenerated holes and a weaker, high-frequency component associated with photogenerated electrons. At 0.13 T, the high-frequency component decays within one period and is not apparent in the FFT. (c) Field dependence of the (top) Larmor frequency,  $ω_L$ , and (bottom) ensemble spin-dephasing times,  $T_2^*$ , for the electron (purple) and hole (red) components. Both precession frequencies increase linearly with increasing magnetic field. The slopes of this field dependence (dashed lines) give  $|g_e| = 1.71$  and  $|g_h| = 0.74$ .  $T_2^*$  for the hole increases slightly upon application of a magnetic field, peaking at 0.13 T before decreasing at larger applied fields. The higher-field data are fitted using eq 2, which yields an ensemble g value distribution characterized by Δg = 0.05. In comparison,  $T_2^*$  for the electron is essentially independent of the magnetic field in this range.

the time domain via the Faraday effect, *i.e.*, by the rotation of a time-delayed linearly polarized probe pulse. Classically, the photogenerated spins precess around the axis of a transverse magnetic field, causing an oscillation of their projection along the laboratory z axis and hence an oscillation in the Faraday rotation angle,  $\theta_{\rm F}$ . This situation corresponds to an oscillating superposition of quantum spin states, quantized along the magnetic field axis. The oscillation frequency (the Larmor frequency,  $\omega_{\rm L}$ ) and the ensemble spin-dephasing time  $(T_2^*)$  can be read out from the frequency of the Faraday rotation amplitude's oscillation and its decay, respectively.

Figure 1d shows TRFR traces collected from a CsPbBr<sub>3</sub> thin film at 4.5 K and various transverse magnetic field strengths  $(B_{\perp})$  up to 0.63 T. The zero-field trace shows a photoinduced Faraday rotation signal that decays within ∼1 ns with pseudobiexponential dynamics. With an applied field, the TRFR traces show a new oscillatory component whose apparent frequency increases with increasing  $B_{\perp}$  and whose amplitude remains enveloped by the zero-field TRFR trace at all fields. Although the fast component of the zero-field TRFR decay is quicker than that of the excitonic PL decay (collected simultaneously, see the Supporting Information), the slow TRFR component decays with essentially the same dynamics as the slow PL decay component. As detailed below, we observe contributions from two distinct spins in the TRFR signal, one decaying quickly and the other decaying slowly. We thus conclude that the fast TRFR decay in Figure 1d reflects spin dephasing of one carrier prior to recombination, and the slow TRFR amplitude decay in Figure 1d reflects spin dynamics of the other photogenerated carrier, with the latter influenced by decay of the carrier population itself under these conditions. In contrast with CsPbBr<sub>3</sub> single crystals,<sup>8</sup> and with recently reported nanocrystals and solution-deposited thin films, 10 there is no longlived TRFR signal that outlives the excitonic PL decay. In those cases, the TRFR signals were all attributed to precession of resident-carrier spins. Instead, these thin-film TRFR dynamics closely resemble those of CsPbBr<sub>3</sub> nanocrystals,

where the TRFR amplitude decay at low temperature is limited by exciton recombination dynamics.

To illustrate the above description, Figure 2a highlights four of the TRFR traces from Figure 1d. At the higher magnetic fields (0.63 and 0.33 T), a distinct field-dependent anomaly is apparent at less than ~100 ps that suggests the presence of two superimposed oscillations in this time window. Figure 2b plots the fast-Fourier transforms (FFTs) of these same four traces, from which two peaks are observed, confirming the presence of two distinct oscillations. The 0.63 T FFT trace shows peaks at 41 and 97 rad ns<sup>-1</sup>. From the relation  $\omega_L = g\mu_B B_\perp/\hbar$ , these peaks correspond to lgl values around 0.7 and 1.7, respectively. The smaller g value agrees reasonably well with those found previously for holes in CsPbBr<sub>3</sub> nanocrystals<sup>9,10</sup> and single crystals<sup>8</sup> as well as with hole g values predicted by firstprinciples calculations.<sup>23</sup> Similarly, the larger g value agrees reasonably well with electron g values measured in singlecrystal and nanocrystalline CsPbBr<sub>3</sub>.8,23-25

To analyze these data more quantitatively, the TRFR traces in Figure 1d are each fitted with the bi-phasic function given in eq 1. Here, the subscripts e and h denote electron and hole species based on the above g values, respectively. Best-fit TRFR traces are included as blue curves along with the experimental traces in Figure 2a. Figure 2c plots the values of  $\omega_{\rm L}$  and  $T_2^*$  extracted from analysis of the full TRFR data set. Electron and hole TRFR trace components are plotted separately in the Supporting Information for illustration. For both the high- and low-frequency components,  $\omega_{\rm L}$  increases linearly with  $B_{\rm L}$ , yielding g values of  $|g_{\rm e}|=1.71$  and  $|g_{\rm h}|=0.74$ , respectively. These values are consistent with those extracted from the FFT of the TRFR curve measured at 0.63 T.

$$\Theta_{F}(t) = A_{e} e^{-t/T_{2,e}^{*}} \cos(\omega_{L,e}t + \phi_{e})$$

$$+ A_{h} e^{-t/T_{2,h}^{*}} \cos(\omega_{L,h}t + \phi_{h})$$
(1)

**Low-Temperature Spin Dephasing.** Figure 2c also plots the field dependence of  $T_2^*$  for the electron and hole signals.

From a value of 282 ps at zero field,  $T_{2, h}^*$  increases with increasing  $B_{\perp}$  to a maximum of 320 ps at 0.13 T (~13% increase) before decreasing again at larger applied fields. This field dependence suggests that inhomogeneous hyperfine fields limit hole-spin coherence times in these thin films. A similar observation was made in nanocrystalline CsPbBr<sub>3</sub>, except the effect of the external magnetic field was much greater in the nanocrystals (~300% increase at 0.13 T), mostly due to the much smaller  $T_{2, h}^*$  at 0 T (~80 ps). This contrast is attributed to the fact that the grain sizes in these CsPbBr3 thin films (60 ± 30 nm lateral edge lengths) are larger than those of the nanocrystals (~10 nm diameter), mitigating the impact of hyperfine-driven dephasing in the former by averaging over a larger number of spin-bearing nuclei. Theory<sup>26</sup> suggests that  $T_2^* \propto \sqrt{N_{\rm L}}$ , where  $N_{\rm L}$  is the number of nuclear spins within the interaction volume of the carriers, consistent with this interpretation. The larger grain volumes in the thin films than in nanocrystals thus lead to a larger  $T_{2, h}^*$  in the absence of  $B_{\perp}$ and to a smaller increase in  $T_{2, h}^*$  at small  $B_{\perp}$ . Because the apparent  $T_{2, h}^*$  is affected by population decay (low-temperature lifetime ~330 ps) in these thin films, the quantitative effect of increasing grain sizes is diminished relative to this simple proportionality. Beyond thin films, the grain sizes in single-crystal CsPbBr3 are assumed to be even larger, and for such samples, application of  $B_{\perp}$  also caused only a small (~17%) increase in  $T_{2, \text{ h}}^*$ . We note the caveat that the pronounced spin heterogeneity reported for the single-crystal CsPbBr<sub>3</sub> sample makes a detailed comparison of hyperfine effects between the single crystals and these vapor-deposited thin films challenging.

The decrease in  $T_{2,\,h}^*$  at  $B_\perp > 0.13$  T shown in Figure 2c is attributed to heterogeneity in the hole g value, characterized by a distribution ( $\Delta g_h$ ) around the mean. This distribution can be analyzed by fitting these data with eq 2, where  $1/T_2^{\rm inh}$  represents the sum of all inhomogeneous contributions to the rate of ensemble spin dephasing. This analysis yields  $\Delta g_h = 0.05$  (7%), which is similar to values of  $\Delta g_h$  observed for CsPbBr<sub>3</sub> nanocrystals and single crystals. This similarity across vastly different morphologies suggests a microscopic origin for the hole's g value heterogeneity, most likely also related to hyperfine interactions. In comparison,  $T_{2,\,e}^*$  does not depend strongly on  $B_\perp$ .

$$1/T_2^* = 1/T_2 + 1/T_2^{\text{inh}} \approx 1/T_2 + \Delta g \mu_B B_L/\hbar$$
 (2)

MCD Analysis of g Values. Previous TRFR investigations of II-VI and III/V semiconductors have used established relationships between exciton g values and electron/hole g values to relate TRFR and magneto-absorption spectroscopic data. TRFR and magneto-absorption spectroscopic data. In lead-halide perovskites, the band-edge CB electron and VB hole both have J = 1/2, and to first order, the exciton g value is described as the sum of the individual electron and hole effective g values (eq 3). Note that TRFR does not allow determination of the signs of the carrier g values, but MCD spectroscopy does allow determination of the sign of  $g_{\rm ex}$ . Equation 3 thus provides an independent test of the identity of the photogenerated spins probed here by TRFR when this experiment is performed in conjunction with MCD measurements.

$$g_{\rm ex} = g_{\rm e} + g_{\rm h} \tag{3}$$

Experimentally, the carrier g (and  $T_2^*$ ) values reported for MHPs have varied widely (see Table S2),  $^{3,8-10,13,24,25}$  and in

most cases, direct comparison with excitonic g values deduced from magneto-absorption or reflectivity measurements has not been made. Such comparison has been made for a CsPbBr<sub>3</sub> single crystal; in this report, the carrier g values detected by TRFR were not directly related to  $g_{\rm ex}$  via eq 3 ( $g_{\rm e}$  = +1.96,  $g_{\rm h}$  = +0.75, and  $g_{\rm ex}$  = +2.4), a discrepancy attributed to exciton dissociation and spatially separated carrier localization. This interpretation was bolstered by the observation of TRFR decay times exceeding the exciton lifetime.

Motivated by the above considerations, we have used magnetic circular dichroism (MCD) spectroscopy to measure  $g_{\rm ex}$  in these vapor-deposited CsPbBr<sub>3</sub> thin films. MCD spectroscopy measures the differential absorption of left and right circularly polarized light induced by a longitudinal magnetic field (Faraday configuration) and provides an accurate measure of excitonic Zeeman splittings as well as other electronic structure information. Figure 3a,b plots the 5

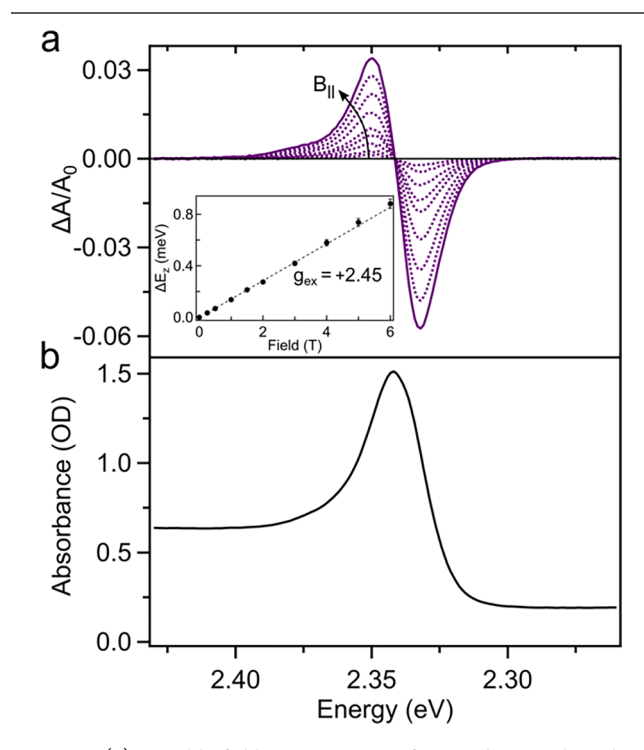


Figure 3. (a) Variable-field MCD spectra of vapor-deposited CsPbBr<sub>3</sub> thin films collected at 5 K. The MCD spectrum is dominated by a derivative-shaped feature that coincides with the first excitonic transition seen in the absorption spectrum. (b) As the longitudinal magnetic field ( $B_{\parallel}$ ) increases, the excitonic Zeeman splitting ( $\Delta E_Z$ ) increases and the MCD intensity for this transition grows. The inset plots the field dependence of  $\Delta E_Z$  measured at 5 K, obtained from quantitative analysis of the MCD and absorption spectra.  $\Delta E_Z$  increases linearly with increasing field. Fitting these data with eq 5 (dashed line) gives  $g_{\rm ex}$  = +2.45 ± 0.04. The low-energy edge of the first excitonic transition in the absorption spectrum comes from an interference fringe (see the Supporting Information for details). The Supporting Information shows the absorption and MCD spectra over a broader energy range.

K MCD spectra of a vapor-deposited CsPbBr<sub>3</sub> thin film measured at several magnetic fields from 0 to 6 T, along with the 5 K, 0 T absorption spectrum of the same film. The absorption maximum at 2.34 eV has an associated derivative-shaped MCD signal centered at the same energy, with a negative leading-edge intensity. Additional weak positive MCD

intensity is observed on the blue edge of the derivative MCD feature, centered around 2.37 eV, a 33 meV splitting. This feature appears too high above the first maximum to be attributable to a longitudinal optical (LO) phonon replica ( $\hbar\omega_{\rm LO}\approx 21~{\rm meV}$ ). A similar feature has been observed in the absorption and reflectance spectra of CsPbBr<sub>3</sub> single crystals and nanocrystals, where it has been attributed to the 2s hydrogen-like excitonic state. Beyond the spectra shown in Figure 3a, only one other MCD feature is observed in our entire spectral window from ~1.55 to ~3.10 eV, namely, a small derivative feature at 3.05 or ~0.7 eV above the first excitonic transition, with MCD intensity ~40× weaker than the first exciton (see the Supporting Information). A transition at this energy has been identified previously as stemming from a van Hove singularity at the M point of the Brillouin zone.

The CsPbBr<sub>3</sub> excitonic MCD intensity increases linearly with increasing magnetic field  $(B_{\parallel})$ , and it is independent of temperature, indicating that it derives from an excited-state Zeeman splitting ( $\Delta E_Z$ ). The leading edge of this MCD feature is negative, corresponding to a positive excited-state g value, i.e.,  $g_{\rm ex} > 0$ . The excitonic Zeeman splitting  $(\Delta E_{\rm Z})$  was determined from analysis of MCD and absorption spectra using eq 4, as detailed previously.<sup>35–37</sup> The derivative-shaped MCD spectrum comes from overlapping positive and negative bands associated with absorption of left and right circularly polarized light, respectively, separated in energy by  $\Delta E_{\rm Z}$ .  $\Delta A$  is defined as  $A_{\rm L} - A_{\rm R}$  according to the sign convention of Piepho and Schatz.35 The first excitonic absorption band is represented by a Gaussian curve with a width of  $2\sigma$  at 1/eof its maximum value,  $A_0$ . Under the rigid-shift approximation, this band's energy splits in a magnetic field but the band shape for left and right circularly polarized absorption remains the same. The MCD peak values now occur at energies  $\sigma/\sqrt{2}$ from the zero-field absorption maximum and have intensities of  $\pm A'/A_0$ . In the analysis here, the negative leading-edge MCD feature was used to quantify  $-A'/A_0$  and  $\sigma$  because the high-energy side of this derivative signal overlaps a second MCD feature of unknown structure. The excitonic Zeeman splitting energy  $(\Delta E_{\rm Z})$  is then deduced from these experimental parameters following eq 4. For example, the 5 K, 6 T MCD spectrum yields  $\Delta E_{\rm Z}$  = +0.87 meV ( $\sigma$  = 13 meV,  $-A'/A_0 = 0.0575$ ). Some uncertainty in  $\Delta E_Z$  arises from ambiguity in the precise parameters describing the absorption band shape (see the Supporting Information), but these parameters are highly constrained by the fact that this absorption peak is very pronounced and by the fact that  $\sigma$  is independently determined from the MCD spectrum.

$$\Delta E_{\rm Z} = -\left(\frac{\sqrt{2e}}{2}\right)\sigma \frac{\Delta A'}{A_0} \tag{4}$$

The inset to Figure 3a plots  $\Delta E_{\rm Z}$  vs the magnetic field obtained from the above analysis. From eq 5, the slope of this plot yields  $g_{\rm ex} = +2.45 \pm 0.04$ . This value agrees well with the sum of TRFR electron and hole g values  $|g_{\rm e}| + |g_{\rm h}| = 1.71 + 0.74 = 2.45$  (eq 3), and in conjunction with the TRFR and excitonic PL decay dynamics discussed above, these results are consistent with assignment of the two precessing spins observed by TRFR to photogenerated band-edge electrons and holes. Moreover, this analysis indicates that  $g_{\rm e}$  and  $g_{\rm h}$  must both be positive in CsPbBr<sub>3</sub>, in agreement with previous conclusions (see the Supporting Information).

$$\Delta E_{\rm Z} = g_{\rm ex} \mu_{\rm B} B_{\parallel} \tag{5}$$

Thermally Activated Spin Dephasing. Returning to the TRFR data, Figure 4a plots the temperature dependence of

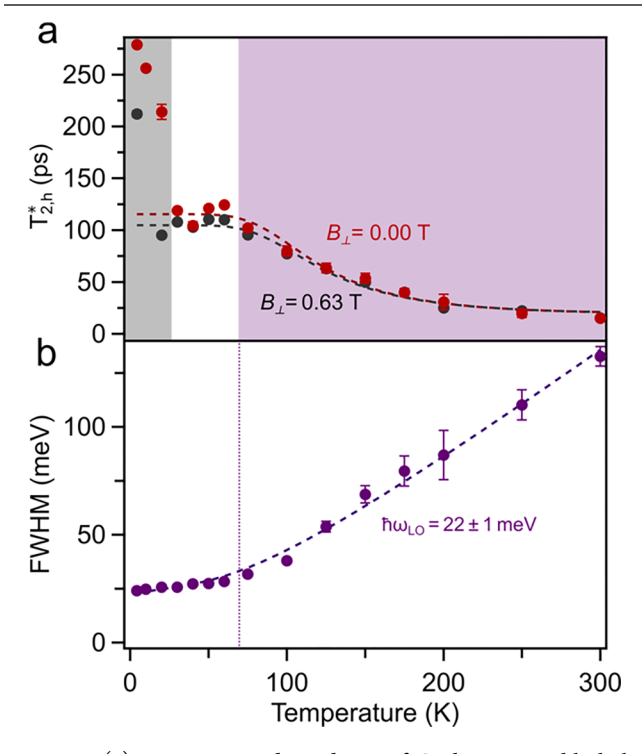


Figure 4. (a) Temperature dependence of CsPbBr<sub>3</sub> ensemble holespin dephasing times  $(T_{2,\,\,\mathrm{h}}^*)$  measured with and without an applied transverse magnetic field. In the low-temperature regime (4.5–30 K, highlighted in gray), both the zero-field and 0.63 T spin-dephasing times decrease rapidly with increasing temperature, and  $T_{2,\,\,\mathrm{h}}^*$  is longer at zero field than at 0.63 T. At higher temperatures, highlighted in purple, thermally activated phonon scattering dominates hole-spin dephasing. (b) Temperature dependence of the PL FWHM for the same CsPbBr<sub>3</sub> thin film. The vertical dotted line at ~75 K highlights the similarity between onset temperatures for the changes in  $T_{2,\,\,\mathrm{h}}^*$  and the PL FWHM. The dashed curves show the results of global analysis of the data in panels (a, b) using eqs 5 and 6, respectively. This global fitting yields  $\hbar\omega_{\mathrm{LO}}=22\pm1$  meV.

 $T_{2,h}^*$  measured with and without an applied magnetic field of 0.63 T. Both data sets show hole spin-coherence times that decrease upon increasing the temperature from 4.5 to  $\sim$ 40 K. Both data sets are then temperature-independent from  $\sim$ 40 to ~75 K before decreasing with increasing temperature up to room temperature, where they both show values of  $T_{2,h}^* \approx 15$ ps (see the Supporting Information). The temperature dependence in this higher-temperature regime, shaded purple in Figure 4a, is interpreted as reflecting thermally activated phonon scattering, as described in eq 6.38 Here,  $\Lambda$  is an attempt frequency and  $F(x) = (1 - \tan h^2(x)) \tan h(x)$ . To test this interpretation, PL linewidths were measured over the same temperature range; PL broadening in CsPbBr<sub>3</sub> is known to stem from exciton coupling with LO phonons.<sup>39</sup> Figure 4b plots the PL full width at half-maximum (FWHM,  $\Gamma$ ) vs temperature. The FWHM is nearly temperature-independent at the lowest temperatures and then increases with increasing temperature above ~75 K. These variable-temperature FWHM data can be described using the independent Boson model<sup>39,40</sup> summarized in eq 7, which reflects the sum of inhomogeneous

PL broadening ( $\Gamma_0$ ), an acoustic phonon interaction term ( $\sigma$ ), and exciton-phonon coupling (with phonon energy  $\hbar\omega_{\rm LO}$ ). The start of the purple region in Figure 4a and the vertical line in Figure 4b are guides to the eye to highlight the temperature ( $\sim$ 75 K) at which both properties begin to change with increasing temperature.

$$T_2^*(T) = \left(\frac{1}{T_2^*(0)} + \Lambda F\left(\frac{\hbar\omega_{\rm LO}}{k_{\rm B}T}\right)\right)^{-1}$$
 (6)

$$\Gamma(T) = \Gamma_0 + \sigma T + \frac{\Gamma_{\text{op}}}{e^{-(\hbar\omega_{\text{LO}}/k_BT)} - 1}$$
(7)

The  $T_{2,h}^*$  and FWHM data in Figure 4 are simultaneously fit to eqs 5 and 6, respectively, linking the LO phonon energy term  $(\hbar\omega_{10})$  between the two equations to provide a global best fit. Note that eq 6 cannot account for the sharp upturn in  $T_{2,h}^*$  below ~40 K (shaded gray in Figure 4a), and those data were excluded from the fitting. The dashed lines in Figure 4a,b show the resulting best-fit curves. This global analysis yields an LO phonon energy of  $\hbar\omega_{\rm LO}$  = 22 ± 1 meV, consistent with reported CsPbBr<sub>3</sub> LO phonon energies (16-36 meV).  $^{8,9,31,41-47}$  For  $T_{2, h}^*$  from 40 K to room temperature, the global fitting further yields  $\Lambda = 0.11 \text{ ps}^{-1}$  and  $T_2^*(0) = 115 \text{ ps}$  for the zero-field data and  $\Lambda = 0.10 \text{ ps}^{-1}$  and  $T_2^*(0) = 104$ ps for  $B_{\perp}$ =0.63 T. For the FWHM data in Figure 4b, the global fitting yields  $\Gamma_0$  = 22 meV,  $\sigma$  ~0.11 meV/K, and  $\Gamma_{op}$  = 104 meV. The best-fit values obtained from this global analysis fall within experimental uncertainty of those extracted from independent fits of the  $T_{2,h}^*$  or FWHM data alone using eqs 6 or 7 (see Figure S11 and Table S1). This analysis supports the conclusion of LO phonon-mediated hole-spin dephasing at elevated temperatures.

Comparison with Other CsPbBr<sub>3</sub> Samples. The results presented here allow comparison of the spin characteristics of these vapor-deposited CsPbBr3 thin films with those of related CsPbBr<sub>3</sub> samples reported previously, specifically, our nanocrystals,9 the nanocrystals and solution-processed polycrystalline thin films of ref 10, and single crystals<sup>8</sup> (see Table S2 of the Supporting Information). Among these samples, the vapordeposited CsPbBr3 thin films reported here are unusual in that they do not show the very large low-temperature  $T_2^*$  values reported for several other CsPbBr3 samples. For example, at 4 K, single-crystal CsPbBr<sub>3</sub> showed  $T_2^*$  values ranging from 0.7 to 1.9 ns, depending on the excitation position on the crystal.8 These large  $T_2^*$  values exceeded the sample's PL lifetime (0.9) ns), allowing the conclusion that the spins probed by TRFR were associated with excess resident charge carriers. The spatial inhomogeneity of  $T_2^*$  was attributed to distributions of resident carriers and traps. Similarly, a very recent comparison of CsPbBr<sub>3</sub> nanocrystals and polycrystalline films<sup>10</sup> also describes low-temperature TRFR oscillations that outlive the sample's PL (e.g.,  $T_{2, h}^* \sim 600$  ps vs  $\tau_{PL} \sim 200$  ps in the nanocrystals), again consistent with those spins being associated with excess resident carriers. In contrast to these observations, the thin films investigated here show rapid electron spin dephasing (less than ~100 ps) even at low temperature, and  $T_{2,h}^*$  appears to be bound by the film's excitonic PL decay time ( $au_{PL}$  ~330 ps, see the Supporting Information). This latter observation strongly suggests that the spin-polarized holes probed by TRFR are the same ones involved in excitonic PL in these thin films, very similar to our earlier conclusion for CsPbBr<sub>3</sub> nanocrystals ( $T_{2, h}^* \sim 300 \text{ ps at } 0.1 \text{ T and } \tau_{PL} \sim 300 \text{ ps}$ ).

These CsPbBr<sub>3</sub> thin films are also unusual in that they show spin coherence up to room temperature. Hole-spin dephasing appears to be accelerated by thermally excited LO phonons in all three forms of CsPbBr<sub>3</sub>, but notably, these vapor-deposited CsPbBr<sub>3</sub> thin films are the only bulk MHP to date to show room-temperature spin coherence ( $T_{2, h}^* \sim 15$  ps). For example, MAPbI<sub>3</sub> thin films,<sup>3</sup> CsPbBr<sub>3</sub> single crystals,<sup>8</sup> and the recently reported solution-processed polycrystalline CsPbBr<sub>3</sub> film<sup>10</sup> all showed spin coherence only at low temperature (less than  $\sim 60$ ,  $\sim 100$ , and  $\sim 50$  K, respectively). In this regard, these vapor-deposited CsPbBr<sub>3</sub> thin films are most similar to our previously reported nanocrystalline CsPbBr<sub>3</sub>, which also showed spin coherence up to room temperature ( $T_{2, h}^* \sim 16$  ps).<sup>9</sup>

At low temperatures, hole-spin dephasing in CsPbBr<sub>3</sub> appears to be dominated by nuclear hyperfine interactions, but these thin films, our nanocrystals,9 and the single crystal8 show markedly different responses to a magnetic field. In all three, application of a small magnetic field ( $B_{\perp} \sim 0.15 \text{ T}$ ) increases  $T_{2,h}^*$  by partially mitigating the inhomogeneous nuclear field, but this increase depends strongly on the sample form: In the nanocrystals,  $T_{2, h}^*$  increases by ~300% under these conditions, whereas in both the thin-film and singlecrystal CsPbBr<sub>3</sub>, the increase is only ~20%. This contrast is interpreted as reflecting the different degrees of the carrier interaction with <sup>207</sup>Pb nuclear spins, given the large Pb 6s orbital character at the valence band edge. For example, this observation could reflect the enhanced carrier mobility in thin films compared to isolated nanocrystals. In this regard, these vapor-deposited CsPbBr3 thin films behave more like bulk single crystals than like nanocrystals, despite having grain lateral edge lengths of only ~60 nm.

Finally, we address the nature of the holes that dominate the TRFR observed here. The very large  $T_2^*$  values reported for some CsPbBr<sub>3</sub> samples <sup>10</sup> exceed  $\tau_{\rm PL}$ , definitively ruling out the association of the observed spins with excitons. In the thin films investigated here and the nanocrystals reported previously, <sup>9</sup> however,  $T_{2,\rm e}^*$  is very short, and not only does  $T_{2,\rm h}^*$  not exceed the PL lifetime, but the PL decay and coherent hole-spin precession show remarkably similar decay dynamics in both samples at ~5 K (see, e.g., Figures S5 and S6). This correlation combined with the g value analysis above strongly suggests that the spins probed by TRFR are indeed associated with the same photogenerated band-edge holes that yield excitonic PL.

No study has yet reported TRFR signals at the exciton g value in any MHP. As emphasized in ref 10, the electron-hole exchange energies in CsPbBr3 nanocrystals are too large to allow independent spin precession of exciton-bound carriers at such low magnetic fields, but these energies could be smaller in bulk. Reference 3 described exciton spin dynamics in CH<sub>3</sub>NH<sub>3</sub>PbI<sub>3</sub> thin films monitored *via* independent precession of exciton-bound electrons and holes. The authors suggested that weakened electron-hole exchange due to charge separation facilitated by the CH<sub>3</sub>NH<sub>3</sub> cations enabled observation of individual carrier spins. For the same perovskite, ref 11 concluded that free excitons convert quickly to localized electrons and holes with retention of their initial spin orientation and that the TRFR is dominated by spin precession of these localized carriers. Reference 28 also described independent electron and hole-spin precession attributed to excitons in Zn<sub>0.80</sub>Cd<sub>0.20</sub>Se quantum wells at field strengths both

above and below those needed to overcome electron-hole exchange but may similarly have involved carrier separation.

TRFR measurements on CsPbBr<sub>3</sub> samples with ample resident carriers (necessarily involving defects) have shown substantially longer low-temperature band-edge electron spincoherence times than observed here, suggesting that the ~40 ps  $T_{2,e}^*$  apparent here is not determined solely by fundamental single-carrier properties such as spin-orbit or hyperfine interactions. Notably, however, CsPbBr3 nanocrystals with no resident carriers and nearly 100% excitonic PL quantum yields also show a similarly short  $T_{2, e}^*$ . The observation of rapid electron-spin decoherence but recombination-limited hole-spin coherence in such nanocrystals could reflect a mechanism involving rapid electron trapping followed by electron detrapping and subsequent radiative electron-hole recombination with still-precessing photogenerated holes. Indeed, reversible carrier trapping has already been demonstrated as important in the PL of brightly emitting MHP and other semiconductor nanocrystals.  $^{48-50}$  Interestingly, CsPbBr $_3$  nanocrystals also show optical coherence times of ~50-80 ps under similar measurement conditions,5 which could hint at a broader influence of rapid (and reversible) electron trapping. Further measurements are required to assess these possibilities.

#### CONCLUSIONS

In summary, coherent spin dynamics in vapor-deposited CsPbBr<sub>3</sub> thin films have been investigated using TRFR spectroscopy. Independent spin-precession signals are observed from both electrons and holes. At low temperatures (~5 K), the electron spins dephase rapidly, whereas the hole spins show much longer coherence times  $(T_{2,h}^* \sim 282 \text{ ps at } 0 \text{ T and})$ 320 ps at 0.13 T), consistent with the CsPbBr<sub>3</sub> band structure, and coherent hole-spin precession appears to be limited by exciton recombination. Hole-spin coherence is still observed even at room temperature ( $T_{2, h}^* \sim 15 \text{ ps}$ ). The carrier g values determined from these measurements agree well with the excitonic g value measured independently by MCD spectroscopy ( $g_{\rm ex}$  = +2.45  $\pm$  0.04). These data also demonstrate that  $g_{\rm e}$ and  $g_h$  are both positive:  $g_e = +1.71$  and  $g_h = +0.74$ . These  $T_{2,h}^*$ values approach the low-temperature exciton PL decay times, suggesting that these TRFR signals arise from the same photogenerated holes responsible for excitonic PL. In addition to offering an attractive platform for exploration of MHP spin physics, the observations reported here also point to vapordeposited CsPbBr3 thin films as a promising morphology for MHP integration into spin-based devices via scalable manufacturing.

### METHODS

**Preparation and General Characterization of CsPbBr**<sub>3</sub> **Thin Films.** CsPbBr<sub>3</sub> thin films were prepared by single-source vapor deposition as described in ref 16. Briefly, cesium bromide (CsBr 99.9%, Alfa Aesar) and lead bromide (PbBr<sub>2</sub> 99.9%, Alfa Aesar) were added to a mortar and pestle in stoichiometric amounts and ground for 10 min until a yellow powder was formed. Film deposition was performed using a home-built evaporator consisting of a bell jar, roughing pump, diffusion pump, and high-current power supply. Approximately 60 mg of the ground powder was loaded onto a Ta evaporation boat. Substrates (c-plane sapphire for TRFR; quartz for MCD) were cleaned sequentially with methanol and acetone. The substrates were mounted 13.5 cm above the evaporation boat. The chamber was evacuated to  $\sim 2 \times 10^{-5}$  Torr, and then, the powder was sublimated by passing a high current through the evaporation boat. The powder was deposited onto the substrates at a rate of  $\sim 1000$  Å/s

over  $\sim$ 2 s. The samples were immediately transferred to a nitrogen-filled glove box for storage until use. Immediately prior to measurement, the samples were annealed in the glove box at 150 °C for 10 min. The thin films on sapphire and quartz used for collection of the spectroscopic data presented in this manuscript were all prepared in parallel in the same evaporation. X-ray diffraction data were collected using a Bruker D8 Discover diffractometer with a I $\mu$ S 2D detector. Scanning electron microscopy (SEM) images were collected using a Thermo Fisher Scientific Apreo S LoVac SEM operated at 5 kV.

Time-Resolved Faraday Rotation. Pump and probe beams were generated by sending the output of a Ti:sapphire laser (Coherent MIRA-HP, pumped by a frequency-doubled Nd3+:YAG laser) pulsed at 76 MHz through an optical parametric oscillator, which generated excitation pulses (~100 fs pulse width). Excitation wavelengths were selected to maximize the TRFR amplitude at each temperature. There was no change in precession frequency or  $T_2^*$  with the pump/probe wavelength. The optimal wavelength shifted from 522 to 528 nm as the temperature decreased due to the anti-Varshni band-gap shift characteristic of CsPbBr3. This output was separated into a pump and probe path using a 50:50 visible beam splitter, and the pump path was subsequently delayed using a mechanical translation stage. The pump beam polarization was then modulated between left and right circular polarizations at a frequency of 50 kHz using a photoelastic modulator (Hinds PEM-90). The pump beam was focused onto the sample (on sapphire) using a 300 mm lens and subsequently blocked after the sample. The probe beam was sent through a linear polarizer before being focused onto the sample with a 300 mm lens. The probe beam overlapped with the pump beam on the sample and was transmitted through an iris. Both beams had a spot size of  $\sim 100 \ \mu m$ , and the probe beam was kept at ~15% of the power of the pump beam using neutral density filter wheels, with average pump powers of 2 mW. After passing through the sample, the polarized probe beam was analyzed using a Wollaston prism and detected using a silicon photodiode bridge. A half-wave plate was placed in front of the Wollaston prism to ensure that the split photodiode channels were balanced in the absence of the pump pulse. Samples were placed in a custom Janis optical cold-finger cryostat, and a transverse magnetic field was applied using an electromagnet (GMW Associates 3470 Dipole). All reported temperatures were measured via a thermocouple affixed ~2 cm above the sample along the copper cold finger. The signal from the split photodiode was measured on a lock-in amplifier (SR830) that triggered off the PEM.

**Magnetic Circular Dichroism.** For helium-temperature MCD and absorption measurements, the CsPbBr<sub>3</sub> vapor-deposited thin film (on quartz) was placed in a superconducting magneto-optical bath cryostat (Cryo-Industries SMC-1659 OVT) oriented in the Faraday geometry. Before measurement, the sample was checked for depolarization by comparing the circular dichroism signal of a chiral standard placed in front of and behind the sample. The depolarization by this thin film was less than ~4%. MCD and absorption signals were collected simultaneously using an Aviv 40DS spectropolarimeter. The MCD signal is reported as  $\Delta A = A_L - A_{R}$ , where  $A_L$  and  $A_R$  refer to the absorbance values of left and right circularly polarized photons in the sign convention of Piepho and Schatz (see the Supporting Information for further details).<sup>35</sup>

Absorption, Photoluminescence, and Related Measurements. Room-temperature absorption spectra were measured using a Cary 500 spectrophotometer. Continuous-wave room-temperature photoluminescence (PL) data were excited using a 405 nm diode and collected using a 0.5 m monochromator (150 g/mm blazed centered at 500 nm) equipped with a CCD. For variable-temperature PL and TRPL measurements, the sample was excited using either the TRFR pump beam (522–528 nm) or a 375 nm Edinburgh diode laser, set to a 20 MHz repetition rate, and PL intensities were measured using a streak camera mounted on a 0.1 m monochromator (150 g/mm blaze centered at 550 nm).

#### ASSOCIATED CONTENT

# **Solution** Supporting Information

The Supporting Information is available free of charge at https://pubs.acs.org/doi/10.1021/acs.chemmater.1c04382.

Details related to grain-size analysis in vapor-deposited thin films, metal-halide perovskite band structure, TRFR curve fitting, PL lifetime and zero-field TRFR comparison, room-temperature thin-film absorption and interference analysis, an extended-range MCD spectrum, and an alternate analysis of the spin-dephasing and FWHM data shown in Figure 4 (PDF)

#### AUTHOR INFORMATION

#### **Corresponding Author**

Daniel R. Gamelin — Department of Chemistry, University of Washington, Seattle, Washington 98195-1700, United States; orcid.org/0000-0003-2888-9916; Email: gamelin@chem.washington.edu

#### Authors

Laura M. Jacoby — Department of Chemistry, University of Washington, Seattle, Washington 98195-1700, United States; © orcid.org/0000-0002-9308-7162

Matthew J. Crane — Department of Chemistry, University of Washington, Seattle, Washington 98195-1700, United States; Present Address: Chemical and Biological Engineering Department, Colorado School of Mines, Golden, CO, 80401; orcid.org/0000-0001-8461-4808

Complete contact information is available at: https://pubs.acs.org/10.1021/acs.chemmater.1c04382

# **Author Contributions**

TL.M.J. and M.J.C. contributed equally to this work.

#### Notes

The authors declare no competing financial interest.

## ACKNOWLEDGMENTS

This work was supported by the Center for Integration of Modern Optoelectronic Materials on Demand (IMOD), a Science and Technology Center supported by the U.S. National Science Foundation under Grant No. DMR-2019444. L.M.J. thanks UW's Clean Energy Institute for graduate fellowship support via the Data Intensive Research Enabling Clean Technology (DIRECT) NSF National Research Traineeship (DGE-1633216), and M.J.C. thanks the Washington Research Foundation for a postdoctoral fellowship. The authors thank the Research Corporation for Science Advancement (RCSA) for supporting this research via a 2021 Cottrell Fellowship award (award #27993) to D.R.G. in support of M.J.C. Thin films were grown using the shared user facilities of UW's Molecular Engineering Materials Center, an NSF MRSEC (DMR-1719797). Sample characterization was conducted in part at UW's Molecular Analysis Facility, a National Nanotechnology Coordinated Infrastructure (NNCI) site at the University of Washington, which is supported in part by funds from the National Science Foundation (awards NNCI-2025489 and NNCI-1542101), the UW Molecular Engineering & Sciences Institute, and the UW Clean Energy Institute. The authors thank C. Erickson for his help with the MCD measurements and analysis.

#### REFERENCES

- (1) Stoumpos, C. C.; Kanatzidis, M. G. The Renaissance of Halide Perovskites and Their Evolution as Emerging Semiconductors. *Acc. Chem. Res.* **2015**, 48, 2791–2802.
- (2) Giovanni, D.; Ma, H.; Chua, J.; Grätzel, M.; Ramesh, R.; Mhaisalkar, S.; Mathews, N.; Sum, T. C. Highly Spin-Polarized Carrier Dynamics and Ultralarge Photoinduced Magnetization in CH<sub>3</sub>NH<sub>3</sub>PbI<sub>3</sub> Perovskite Thin Films. *Nano Lett.* **2015**, *15*, 1553–1558
- (3) Odenthal, P.; Talmadge, W.; Gundlach, N.; Wang, R.; Zhang, C.; Sun, D.; Yu, Z.-G.; Valy Vardeny, Z.; Li, Y. S. Spin-polarized exciton quantum beating in hybrid organic—inorganic perovskites. *Nat. Phys.* **2017**, *13*, 894—899.
- (4) Zhai, Y.; Baniya, S.; Zhang, C.; Li, J.; Haney, P.; Sheng, C.-X.; Ehrenfreund, E.; Vardeny, Z. V. Giant Rashba splitting in 2D organic-inorganic halide perovskites measured by transient spectroscopies. *Sci. Adv.* **2017**, *3*, No. e1700704.
- (5) Utzat, H.; Sun, W.; Kaplan, A. E. K.; Krieg, F.; Ginterseder, M.; Spokoyny, B.; Klein, N. D.; Shulenberger, K. E.; Perkinson, C. F.; Kovalenko, M. V.; Bawendi, M. G. Coherent single-photon emission from colloidal lead halide perovskite quantum dots. *Science* **2019**, *363*, 1068–1072.
- (6) Strohmair, S.; Dey, A.; Tong, Y.; Polavarapu, L.; Bohn, B. J.; Feldmann, J. Spin Polarization Dynamics of Free Charge Carriers in CsPb1, Nanocrystals. *Nano Lett.* **2020**, *20*, 4724–4730.
- (7) Spencer, M. S.; Fu, Y.; Schlaus, A. P.; Hwang, D.; Dai, Y.; Smith, M. D.; Gamelin, D. R.; Zhu, X.-Y. Spin-Orbit Coupled Exciton-Polariton Condensates in Lead Halide Perovskites. *Sci. Adv.* **2021**, *7*, No. eabi7667.
- (8) Belykh, V. V.; Yakovlev, D. R.; Glazov, M. M.; Grigoryev, P. S.; Hussain, M.; Rautert, J.; Dirin, D. N.; Kovalenko, M. V.; Bayer, M. Coherent spin dynamics of electrons and holes in CsPbBr<sub>3</sub> perovskite crystals. *Nat. Commun.* **2019**, *10*, *673*.
- (9) Crane, M. J.; Jacoby, L. M.; Cohen, T. A.; Huang, Y.; Luscombe, C. K.; Gamelin, D. R. Coherent Spin Precession and Lifetime-Limited Spin Dephasing in CsPbBr<sub>3</sub> Perovskite Nanocrystals. *Nano Lett.* **2020**, 20, 8626–8633.
- (10) Grigoryev, P. S.; Belykh, V. V.; Yakovlev, D. R.; Lhuillier, E.; Bayer, M. Coherent Spin Dynamics of Electrons and Holes in CsPbBr<sub>3</sub> Colloidal Nanocrystals. *Nano Lett.* **2021**, *21*, 8481–8487.
- (11) Garcia-Arellano, G.; Trippé-Allard, G.; Legrand, L.; Barisien, T.; Garrot, D.; Deleporte, E.; Bernardot, F.; Testelin, C.; Chamarro, M. Energy Tuning of Electronic Spin Coherent Evolution in Methylammonium Lead Iodide Perovskites. *J. Phys. Chem. Lett.* **2021**, *12*, 8272–8279.
- (12) Kim, Y.-H.; Zhai, Y.; Lu, H.; Pan, X.; Xiao, C.; Gaulding, E. A.; Harvey, S. P.; Berry, J. J.; Vardeny, Z. V.; Luther, J. M.; Beard, M. C. Chiral-induced spin selectivity enables a room-temperature spin light-emitting diode. *Science* **2021**, *371*, 1129.
- (13) Wang, J.; Zhang, C.; Liu, H.; McLaughlin, R.; Zhai, Y.; Vardeny, S. R.; Liu, X.; McGill, S.; Semenov, D.; Guo, H.; Tsuchikawa, R.; Deshpande, V. V.; Sun, D.; Vardeny, Z. V. Spin-optoelectronic devices based on hybrid organic-inorganic trihalide perovskites. *Nat. Commun.* **2019**, *10*, 1–6.
- (14) Protesescu, L.; Yakunin, S.; Bodnarchuk, M. I.; Krieg, F.; Caputo, R.; Hendon, C. H.; Yang, R. X.; Walsh, A.; Kovalenko, M. V. Nanocrystals of Cesium Lead Halide Perovskites (CsPbX<sub>3</sub>, X = Cl, Br, and I): Novel Optoelectronic Materials Showing Bright Emission with Wide Color Gamut. *Nano Lett.* **2015**, *15*, 3692–3696.
- (15) Akbulatov, A. F.; Luchkin, S. Y.; Frolova, L. A.; Dremova, N. N.; Gerasimov, K. L.; Zhidkov, I. S.; Anokhin, D. V.; Kurmaev, E. Z.; Stevenson, K. J.; Troshin, P. A. Probing the Intrinsic Thermal and Photochemical Stability of Hybrid and Inorganic Lead Halide Perovskites. J. Phys. Chem. Lett. 2017, 8, 1211–1218.
- (16) Crane, M. J.; Kroupa, D. M.; Roh, J. Y.; Anderson, R. T.; Smith, M. D.; Gamelin, D. R. Single-Source Vapor Deposition of Quantum-Cutting Yb<sup>3+</sup>:CsPb(Cl<sub>1-x</sub>Br<sub>x</sub>)<sub>3</sub> and Other Complex Metal-Halide Perovskites. ACS Appl. Energy Mater. **2019**, 2, 4560–4565.

- (17) Kroupa, D. M.; Crane, M. J.; Gamelin, D. R. In Single-source flash sublimation of metal-halide semiconductors; Physical Chemistry of Semiconductor Materials and Interfaces XVIII, 2019/09/16/; International Society for Optics and Photonics: 2019; p 110840J.
- (18) Dyakonov, M. I. Basics of Semiconductor and Spin Physics. In *Spin Physics in Semiconductors*; Dyakonov, M. I., Ed. Springer: Berlin, Heidelberg, 2008; pp. 1–28.
- (19) Cleveland, I. J.; Tran, M. N.; Dey, A.; Aydil, E. S. Vapor deposition of CsPbBr<sub>3</sub> thin films by evaporation of CsBr and PbBr<sub>2</sub>. *J. Vac. Sci. Technol., A* **2021**, *39*, No. 043415.
- (20) Crooker, S. A.; Awschalom, D. D.; Samarth, N. Time-resolved Faraday rotation spectroscopy of spin dynamics in digital magnetic heterostructures. *IEEE J. Sel. Top. Quantum Electron.* **1995**, *1*, 1082–1092.
- (21) Awschalom, D. D.; Kikkawa, J. M. Electron Spin and Optical Coherence in Semiconductors. *Phys. Today* **1999**, *52*, 33.
- (22) Yakovlev, D. R.; Bayer, M. Coherent Spin Dynamics of Carriers. In *Spin Physics in Semiconductors*; Dyakonov, M. I. Ed. Springer: Berlin, Heidelberg, 2008; pp. 135–177.
- (23) Yu, Z. G. Effective-mass model and magneto-optical properties in hybrid perovskites. *Sci. Rep.* **2016**, *6*, 28576.
- (24) Canneson, D.; Shornikova, E. V.; Yakovlev, D. R.; Rogge, T.; Mitioglu, A. A.; Ballottin, M. V.; Christianen, P. C. M.; Lhuillier, E.; Bayer, M.; Biadala, L. Negatively Charged and Dark Excitons in CsPbBr<sub>3</sub> Perovskite Nanocrystals Revealed by High Magnetic Fields. *Nano Lett.* **2017**, *17*, 6177–6183.
- (25) Fu, M.; Tamarat, P.; Huang, H.; Even, J.; Rogach, A. L.; Lounis, B. Neutral and Charged Exciton Fine Structure in Single Lead Halide Perovskite Nanocrystals Revealed by Magneto-optical Spectroscopy. *Nano Lett.* **2017**, *17*, 2895–2901.
- (26) Merkulov, I. A.; Efros, A. L.; Rosen, M. Electron spin relaxation by nuclei in semiconductor quantum dots. *Phys. Rev. B* **2002**, *65*, 205309.
- (27) Snelling, M. J.; Blackwood, E.; McDonagh, C. J.; Harley, R. T.; Foxon, C. T. B. Exciton, heavy-hole, and electron g factors in type-I GaAs/Al<sub>2</sub>Ga<sub>1-x</sub>As quantum wells. *Phys. Rev. B* **1992**, 45, 3922–3925.
- (28) Harley, R. T. Spin-Related Effects in III-V Semiconductors. In *Coherent Optical Interactions in Semiconductors*; Phillips, R. T. Ed. Springer US: Boston, MA, 1994; pp. 91–109.
- (29) Crooker, S. A.; Awschalom, D. D.; Baumberg, J. J.; Flack, F.; Samarth, N. Optical spin resonance and transverse spin relaxation in magnetic semiconductor quantum wells. *Phys. Rev. B* **1997**, *56*, 7574–7588.
- (30) Gupta, J. A.; Awschalom, D. D.; Efros, A. L.; Rodina, A. V. Spin dynamics in semiconductor nanocrystals. *Phys. Rev. B* **2002**, *66*, 125307.
- (31) Iaru, C. M.; Geuchies, J. J.; Koenraad, P. M.; Vanmaekelbergh, D.; Silov, A. Y. Strong Carrier—Phonon Coupling in Lead Halide Perovskite Nanocrystals. *ACS Nano* **2017**, *11*, 11024—11030.
- (32) Heidrich, K.; Schäfer, W.; Schreiber, M.; Söchtig, J.; Trendel, G.; Treusch, J.; Grandke, T.; Stolz, H. J. Electronic structure, photoemission spectra, and vacuum-ultraviolet optical spectra of CsPbCl<sub>3</sub> and CsPbBr<sub>3</sub>. *Phys. Rev. B* **1981**, 24, 5642–5649.
- (33) Ramade, J.; Andriambariarijaona, L. M.; Steinmetz, V.; Goubet, N.; Legrand, L.; Barisien, T.; Bernardot, F.; Testelin, C.; Lhuillier, E.; Bramati, A.; Chamarro, M. Fine structure of excitons and electronhole exchange energy in polymorphic CsPbBr<sub>3</sub> single nanocrystals. *Nanoscale* **2018**, *10*, 6393–6401.
- (34) Dendebera, M.; Chornodolskyy, Y.; Gamernyk, R.; Antonyak, O.; Pashuk, I.; Myagkota, S.; Gnilitskyi, I.; Pankratov, V.; Vistovskyy, V.; Mykhaylyk, V.; Grinberg, M.; Voloshinovskii, A. Time resolved luminescence spectroscopy of CsPbBr<sub>3</sub> single crystal. *J. Lumin.* **2020**, 225, 117346.
- (35) Piepho, S. B.; Schatz, P. N. Group theory in spectroscopy: with applications to magnetic circular dichroism; John Wiley & Sons, Ltd: New York, 1983.
- (36) Hoffman, D. M.; Meyer, B. K.; Ekimov, A. I.; Merkulov, I. A.; Efros, A. L.; Rosen, M.; Couino, G.; Gacoin, T.; Boilot, J. P. Giant

ı

- internal magnetic fields in Mn doped nanocrystal quantum dots. *Solid State Commun.* **2000**, *114*, 547–550.
- (37) Barrows, C. J.; Vlaskin, V. A.; Gamelin, D. R. Absorption and Magnetic Circular Dichroism Analyses of Giant Zeeman Splittings in Diffusion-Doped Colloidal Cd<sub>1-x</sub>Mn<sub>x</sub>Se Quantum Dots. *J. Phys. Chem. Lett.* **2015**, *6*, 3076–3081.
- (38) Semenov, Y. G.; Kim, K. W. Elastic spin-relaxation processes in semiconductor quantum dots. *Phys. Rev. B* **2007**, *75*, 195342.
- (39) Saran, R.; Heuer-Jungemann, A.; Kanaras, A. G.; Curry, R. J. Giant Bandgap Renormalization and Exciton—Phonon Scattering in Perovskite Nanocrystals. *Adv. Opt. Mater.* **2017**, *5*, 1700231.
- (40) Rudin, S.; Reinecke, T. L. Temperature-dependent exciton linewidths in semiconductor quantum wells. *Phys. Rev. B* **1990**, *41*, 3017–3027.
- (41) Steele, J. A.; Puech, P.; Monserrat, B.; Wu, B.; Yang, R. X.; Kirchartz, T.; Yuan, H.; Fleury, G.; Giovanni, D.; Fron, E.; Keshavarz, M.; Debroye, E.; Zhou, G.; Sum, T. C.; Walsh, A.; Hofkens, J.; Roeffaers, M. B. J. Role of Electron—Phonon Coupling in the Thermal Evolution of Bulk Rashba-Like Spin-Split Lead Halide Perovskites Exhibiting Dual-Band Photoluminescence. *ACS Energy Lett.* **2019**, *4*, 2205–2212.
- (42) Wei, K.; Xu, Z.; Chen, R.; Zheng, X.; Cheng, X.; Jiang, T. Temperature-dependent excitonic photoluminescence excited by two-photon absorption in perovskite CsPbBr<sub>3</sub> quantum dots. *Opt. Lett.* **2016**, *41*, 3821–3824.
- (43) Lao, X.; Yang, Z.; Su, Z.; Wang, Z.; Ye, H.; Wang, M.; Yao, X.; Xu, S. Luminescence and thermal behaviors of free and trapped excitons in cesium lead halide perovskite nanosheets. *Nanoscale* **2018**, *10*, 9949–9956.
- (44) Guo, Y.; Yaffe, O.; Hull, T. D.; Owen, J. S.; Reichman, D. R.; Brus, L. E. Dynamic emission Stokes shift and liquid-like dielectric solvation of band edge carriers in lead-halide perovskites. *Nat. Commun.* **2019**, *10*, 1175.
- (45) Lao, X.; Zhou, W.; Bao, Y.; Wang, X.; Yang, Z.; Wang, M.; Xu, S. Photoluminescence signatures of thermal expansion, electron—phonon coupling and phase transitions in cesium lead bromide perovskite nanosheets. *Nanoscale* **2020**, *12*, 7315—7320.
- (46) Yuan, Y.; Chen, M.; Yang, S.; Shen, X.; Liu, Y.; Cao, D. Exciton recombination mechanisms in solution grown single crystalline CsPbBr<sub>3</sub> perovskite. *J. Lumin.* **2020**, 226, 117471.
- (47) Shibata, K.; Yan, J.; Hazama, Y.; Chen, S.; Akiyama, H. Exciton Localization and Enhancement of the Exciton—LO Phonon Interaction in a CsPbBr<sub>3</sub> Single Crystal. *J. Phys. Chem. C* **2020**, 124, 18257—18263.
- (48) Whitham, P. J.; Marchioro, A.; Knowles, K. E.; Kilburn, T. B.; Reid, P. J.; Gamelin, D. R. Single-Particle Photoluminescence Spectra, Blinking, and Delayed Luminescence of Colloidal CuInS<sub>2</sub> Nanocrystals. *J. Phys. Chem. C* **2016**, *120*, 17136–17142.
- (49) Chirvony, V. S.; González-Carrero, S.; Suárez, I.; Galian, R. E.; Sessolo, M.; Bolink, H. J.; Martínez-Pastor, J. P.; Pérez-Prieto, J. Delayed Luminescence in Lead Halide Perovskite Nanocrystals. *J. Phys. Chem. C* **2017**, *121*, 13381–13390.
- (50) Wang, Y.; Zhi, M.; Chan, Y. Delayed Exciton Formation Involving Energetically Shallow Trap States in Colloidal CsPbBr<sub>3</sub> Quantum Dots. *J. Phys. Chem. C* **2017**, *121*, 28498–28505.